Journal of
Materials Chemistry A

Accepted Manuscript

Volume 4 | Number 1 | 7 January 2016 | Pages 1–330

Journal of
Materials Chemistry A

Materials for energy and sustainability
www.rsc.org/MaterialsA

ISSN 2050-7488

ROYAL SOCIETY
OF CHEMISTRY

PAPER
Kun Chang, Zhaorong Chang et al.
Bubble-template-assisted synthesis of hollow fullerene-like
MoS₂ nanocages as a lithium ion battery anode material

175 YEARS

ROYAL SOCIETY
OF CHEMISTRY

rsc.li/materials-a

1   **Ultrathin Petal-like NiAl Layered Double Oxide/Sulfide Composites as Advanced**

2   **Electrode for High-performance Asymmetric Supercapacitor**

3

4   Lei Li[a], Kwan San Hui[b*], Kwun Nam Hui[c*], and Young Rae Cho[a*]

5

6

7   [a] School of Materials Science and Engineering, Pusan National University, San 30 Jangjeon-

8   dong, Geumjeong-gu, Busan 609-735, Republic of Korea

9   [b] School of Mathematics, University of East Anglia, Norwich, NR4 7TJ, United Kingdom

10   [c] Institute of Applied Physics and Materials Engineering, University of Macau, Avenida da

11   Universidade, Macau, China

12

13

14   *Corresponding author:

15   E-mail: k.hui@uea.ac.uk (Kwan San Hui)

16   E-mail: bizhui@umac.mo (Kwun Nam Hui)

17   E-mail: yescho@pusan.ac.kr (Young Rae Cho)

18

19

20

21

22

23

24

1   **Abstract**

2   Layered double hydroxide (LDH) is an important layer-structured material for

3   supercapacitors because of its versatile compositions, high theoretical capacitance,

4   environmental friendliness, and low cost. However, the high resistivity of this material results

5   in capacity fading, limiting its application in energy storage. Herein, we develop a facile

6   approach to synthesize ultrathin petal-like NiAl layered double oxide/sulfide (LDO/LDS)

7   composites with high electrochemical activity using hydrothermal reaction followed by

8   sulfidation process. Scanning electron micrograph shows that the petal-like NiAl LDO/LDS

9   composites are as thin as ~10 nm with a mean lateral dimension of ~1 μm. The NiAl

10   LDO/LDS electrode delivers remarkably high specific capacitance of 2250.5 F g^{-1} at 1 A g^{-1}

11   compared with that of NiAl LDH (1740.5 F g^{-1} at 1 A g^{-1}) and possesses good cycling ability

12   of 88.9% capacitance retention over 5000 cycles at 5 A g^{-1}. Asymmetric supercapacitor (ASC)

13   is fabricated using NiAl LDO/LDS and graphene as positive and negative electrodes,

14   respectively. NiAl LDO/LDS//G ASC exhibits specific capacitance of 153.3 F g^{-1} at 1 A g^{-1},

15   high energy density of 47.9 Wh kg^{-1} at a power density of 750 W kg^{-1}, and reliable cycling

16   stability of 95.68% capacitance retention after 5000 cycles. Results highlight that NiAl

17   LDO/LDS composites are promising materials for energy storage devices with long cycling

18   stability.

19

22

23

24

1

1. Introduction

Supercapacitors have electric double-layer capacitors generally composed of carbonaceous materials based on electrostatic adsorption/desorption. Pseudocapacitors utilizing transition metal oxides/hydroxides based on Faradaic reactions are advantageous because of their high power density, fast charge propagation dynamics, and long cycle life compared with batteries.[1-4] Among transitional metal oxides, layered double hydroxide (LDH) consisting of brucite-like host layers and charge-compensating interlayer anions has attracted significant attention as promising electrode materials in electrochemistry because of their high redox activity, relatively low cost, and environmental friendliness.[5-8] The general formula of LDHs can be described as $[M_{1-x}^{2+}M_x^{3+}(OH)_2](A^{n-})_{x/n}\cdot mH_2O$, where M^{2+} indicates the divalent cation (Ni^{2+}, Co^{2+}, Cu^{2+}, Zn^{2+}, Mg^{2+}, etc.), M^{3+} indicates the trivalent cation (Al^{3+}, Mn^{3+}, Cr^{3+}, Fe^{3+}, etc.), and A^{n-} indicates the interlayer exchangeable anion (OH^-, SO^{4-}, NO^{3-}, etc.).[9, 10] Based on the layered structure, electrical double-layer capacitance can be obtained by the abundant slabs in the structure, while Faradaic reactions can be achieved at the surface of the electroactive sites for charge storage.[5, 8] Therefore, LDH materials hold the great potential for achieving high energy density and power density simultaneously compared with other supercapacitive electrode materials.[8, 11, 12] However, the high electrical resistivity of LDH adversely affects the electron transfer kinetics, resulting in poor cycling stability. This characteristic impedes the potential of LDH in commercial applications.[5, 13-15]

Morphology engineering is an effective approach to improve the electrochemical performance of electrode materials. For example, ultrathin mesoporous nanostructures, such as NiO,[16, 17] Co_3O_4,[18] and $NiCo_2O_4$[19], have been reported to demonstrate high specific

1   capacitance, high-rate capability, and excellent cycling performance in energy storage

2   applications, because huge electroactive sites on the exposed surface are available for

3   electrochemical reaction with electrolyte ions.[20] Meanwhile, sulfidation to convert low

4   electrical conductive metal oxide to high electrical conductive metal sulfide has been reported.

5   Electrochemical performance of electrode materials is enhanced because of the higher

6   electrical conductivity of sulfide-based oxides.[21, 22] Pu et al. reported $NiCo_2S_4$ nanotubes

7   arrays on Ni foam exhibiting high specific capacitance of 738 F g^{-1} at 4 A g^{-1} with excellent

8   rate capability of 78% capacitance retention at 32 A g^{-1} and good cycling stability showing

9   retention capacity of 93.4 % after 4000 cycles.[23] Hou et al. reported Ni_7S_6/Co_3O_4 nanoboxes

10   with intriguing pseudocapacitance that delivered a remarkable specific capacitance of 677 F

11   g^{-1} at 4 A g^{-1}.[24] However, electrochemical properties of sulfide-based NiAl-LDH are rarely

12   reported. Herein, we report a facile approach to synthesize NiAl layered double oxide/sulfide

13   composites (LDO/LDS) with high electrochemical activity using hydrothermal reaction

14   followed by sulfidation process. For comparison, electrochemical performance of NiAl LDH

15   synthesized without sulfidation was also compared. The NiAl LDO/LDS electrode delivers

16   remarkably high specific capacitance of 2250.5 F g^{-1} at 1 A g^{-1} compared with that of NiAl

17   LDH (1740.5 F g^{-1} at 1 A g^{-1}) and possesses good cycling ability of 88.9% capacitance

18   retention over 5000 cycles at 5 A g^{-1}. An asymmetric supercapacitor (ASC) was fabricated

19   using NiAl LDO/LDS and graphene as positive and negative electrodes, respectively. NiAl

20   LDO/LDS//G ASC exhibits specific capacitance of 153.3 F g^{-1} at 1 A g^{-1}, high energy density

21   of 47.9 Wh kg^{-1} at a power density of 750 W kg^{-1}, and reliable cycling stability of 95.68%

22   capacitance retention after 5000 cycles. Hence, the petal-like NiAl LDO/LDS composites

23   may serve as a promising electrode material for many potential applications such as

24   photocatalysts, electrocatalysts, batteries because of its excellent physical and chemical

Journal of Materials Chemistry A Accepted Manuscript

1   properties.[25, 26]

2

3   **2. Experimental details**

4   **2.1 Synthesis of petal-like NiAl LDH nanosheets**

5   Nickel nitrate hexahydrate ($Ni(NO_3)_2 \cdot 6H_2O$), aluminum nitrate nonahydrate

6   ($Al(NO_3)_3 \cdot 9H_2O$), sodium thiosulfate ($Na_2S_2O_3$), and urea (($NH_2)_2CO$) were purchased from

7   Sigma Aldrich (USA). Acetone and anhydrous ethanol were purchased from SK Chemical

8   (South Korea). All chemicals were of analytical grade and used without further purification.

9   The petal-like NiAl LDH nanosheets were synthesized using a simple hydrothermal

10 method.[24] $Ni(NO_3)_2 \cdot 6H_2O$ (0.003 mol) and $Al(NO_3)_3 \cdot 9H_2O$ (0.001 mol) were dissolved in

11 30 mL of deionized (DI) water with vigorous stirring for 15 min. Subsequently, urea (0.015

12 mol) was added into the mixture and stirred for another 15 min. Then, the solution was

13 transferred to a 50 mL Teflon-lined autoclave and kept at 120 °C for 12 h. After cooling

14 down to room temperature, the as-synthesized product was taken and rinsed using DI water

15 and ethanol, followed by drying at 80 °C for 12 h.

16

17 **2.2. Preparation of petal-like NiAl LDO/LDS composites**

18 NiAl LDO/LDS was prepared by mixing as-prepared NiAl LDH powder with $Na_2S_2O_3$ at a

19 mole ratio of 1:2, and the mixture was manually ground for 30 min in an agate mortar.

20 Subsequently, the mixed powder was transferred in a quartz tube and heated in high-purity

21 argon gas atmosphere at 400, 500, 600, and 700 °C for 12 h. After cooling down to room

22 temperature, the black color NiAl LDO/LDS composites were washed several times with

23 ethanol to prevent the hydrolysis of Al_2S_3 to $Al(OH)_3$ and H_2S and drying at 80 °C for 12 h.

24

1   **2.3. Preparation of graphene**

2   Graphite oxide was prepared using natural graphite (Asbury Carbons) through the modified

3   Hummers method as reported elsewhere.[27, 28] Similar to a typical experiment, graphite flakes

4   (3.0 g) were stirred in concentrated sulfuric acid (70 mL) at room temperature, followed by

5   the addition of sodium nitrate (1.5 g). Potassium permanganate (9.0 g) was added slowly to

6   keep the solution temperature lower than 20 °C while maintaining the reaction flask in an ice

7   bath. The entire reaction system was subsequently placed into a 35 °C water bath for 30 min,

8   and slurry was formed. Afterward, 140 mL of DI water was added to the slurry, and the

9   suspension was stirred for another 15 min. The solution was diluted with additional DI water

10 (500 mL) and treated with 20 mL of H_2O_2 (30 wt%) until no gas was produced. The solution

11 color changed from brown into yellow. The mixture was filtered and washed with 1:10 HCl

12 aqueous solution (250 mL) to provide the graphene oxide solution. Graphene was obtained by

13 a hydrothermal reaction of the graphene oxide solution (2 mg mL^{-1}, 40 mL) in a 50 mL

14 Teflon-lined autoclave and kept at 180 °C for 10 h. The product was cleaned with ethanol and

15 water and freeze-dried overnight.

16

17 **2.4. Material characterization**

18 X-ray diffraction (XRD) patterns were recorded using a Bruker D8 Advanced X-Ray

19 Diffractometer with Ni-filtered Cu Kα radiation (λ = 1.5406 Å) at voltage of 40 kV and

20 current of 200 mA. The composition and valence states of the prepared samples were

21 analyzed by X-ray photoelectron spectroscopy (XPS, VG Scientifics ESCALAB250), and the

22 instrument was calibrated to the carbon peak C 1s at 284.6 eV. Field-emission scanning

23 electron microscopy (FESEM) images were acquired using Hitachi S−4800. Transmission

24 electron microscopy (TEM) images were obtained using Talos F200 X. Scanning

1 transmission electron microscopy with energy dispersive X-ray spectroscopy (EDS) (Talos

2 F200 X) mapping was performed to identify the distributions of Ni, Al, O, and S.

3

4 **2.5. Electrochemical measurements**

5 Electrochemical measurements were conducted in a three-electrode electrochemical system

6 containing 6 M KOH as electrolyte at room temperature. The active material on nickel foam

7 (1 cm×1 cm) was selected as the working electrode. Platinum foil and a saturated calomel

8 electrode (SCE) were used as the counter and reference electrodes, respectively. Cyclic

9 voltammetry (CV) and galvanostatic charge/discharge (GCD) were performed on an Ivium-n-

10 Stat electrochemical workstation (Ivium, Netherlands). Electrochemical impedance spectrum

11 (EIS) measurements were conducted in the frequency range of 100 kHz to 0.1 Hz in the open

12 circuit potential with alternating current perturbation of 5 mV.

13

14 **Fabrication of the NiAl LDO/LDS//G ASC**

15 The ASCs were packaged in a CR 2302 coin cell. In this cell, NiAl LDO/LDS electrode,

16 graphene electrode, cellulose fabric, and 6 M KOH solution were used as the positive

17 electrode, negative electrode, separator, and electrolyte, respectively. The positive and

18 negative electrodes were prepared as follows. The prepared active materials, acetylene black,

19 and polytetrafluoroethylene in mass proportion of 75:20:5 were mixed by adding a small

20 amount of ethanol to produce a homogeneous mash. The mass loadings of the NiAl LDO/LD

21 S and graphene samples were determined to be 1.5 and 7.5 mg, respectively. Then, the

22 resulting slurry was coated onto a nickel foam current collector. Finally, the fabricated

23 electrode was pressed and dried at 80 °C overnight and was then cut into a round film. The

24 mass loading ratio of NiAl LDO/LDS to graphene was balanced to be approximately 0.20 to

1 obtain optimized electrochemical performance. Specific capacitance (C_{device}), energy density

2 (E), and power density (P) were calculated from the GCD curves according to the following

3 equations [29]:

$$C_{device} = \frac{I \times \Delta t}{\Delta V \times M} \tag{1}$$

$$E = \frac{1}{2} C_{device} \Delta V^2 \tag{2}$$

$$P = \frac{E}{\Delta t} \tag{3}$$

7 where I is the discharge current (A), Δt is the discharge time (s), M is the electrode

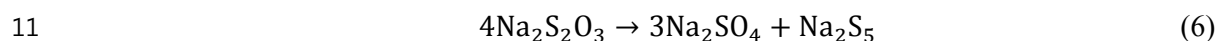8 mass (g), and ΔV is the operating potential window of the device (V).
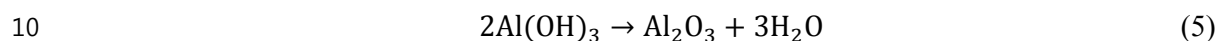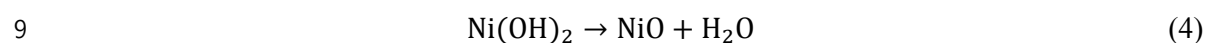
9

10 **3. Results and discussion**
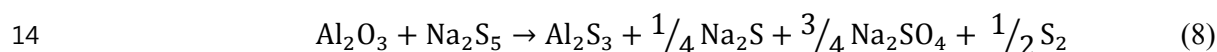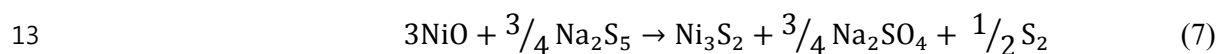
11 **3.1. Material characterization**

12 Fig. 1a shows the XRD pattern of the NiAl LDH. Well-defined main diffraction peaks are

13 displayed at 11.7°, 23.5°, 35.1°, 39.7°, 47.3°, 61.2°, 62.5°, and 66.5° which can be indexed as

14 the (003), (006), (012), (015), (018), (110), (113), and (116) crystal planes of NiAl LDH

15 (JCPDS 15-0087).[30, 31] Fig. 1b shows the XRD spectra of the as-obtained NiAl LDO/LDS

16 composites contained at sulfidation temperature of 500 °C, which are indexed to the

17 diffraction planes of Ni_3S_2 (JCPDS 44-1418), NiO (JCPDS 01-1239), and Al_2S_3 (JCPDS 47-

18 1313).[32, 33] This result confirms the successful conversion of NiAl LDH to NiAl LDO/LDS.

19 Scheme 1 displayed the sulfidation of NiAl LDH occurs during the thermal annealing process

20 with sulfide source. Meanwhile, the XRD patterns and the corresponding SEM images of the

21 NiAl LDO/LDS composites obtained at various sulfidation temperature (400, 600, and

22 700 °C) were shown in Fig. S1. When the sulfidation temperature increases, the crystallinity

23 of the NiAl LDO/LDS composites increases, signifying by the increasing intensity of the

24 (110) peaks of the Ni_3S_2 phase (Fig. S1a). At sulfidation temperature of 700 °C, the NiO

1   peaks disappear, and the pure NiAl LDS is formed. However, the morphology of the NiAl

2   LDO/LDS composites degrades at 600 °C (Fig. S1c) and aggregates to form a particle-like

3   morphology when the sulfidation temperature reaches 700 °C (Fig. S1d). Hence, the NiAl

4   LDO/LDS composites obtained at sulfidation temperature of 500 °C exhibits intact petal-like

5   morphology and desirable LDS characteristics, which is selected as the optimized NiAl

6   LDO/LDS composites in this study. The hierarchical petal-like NiAl LDO/LDS LDO/LDS

7   composites are formed according to the following reactions.[34, 35]

8   **Decomposition process**

9
$$Ni(OH)_2 \rightarrow NiO + H_2O \tag{4}$$

10
$$2Al(OH)_3 \rightarrow Al_2O_3 + 3H_2O \tag{5}$$

11
$$4Na_2S_2O_3 \rightarrow 3Na_2SO_4 + Na_2S_5 \tag{6}$$

12   **Synthetic process**

13
$$3NiO + {}^{3}\!/_{4}\,Na_2S_5 \rightarrow Ni_3S_2 + {}^{3}\!/_{4}\,Na_2SO_4 + {}^{1}\!/_{2}\,S_2 \tag{7}$$

14
$$Al_2O_3 + Na_2S_5 \rightarrow Al_2S_3 + {}^{1}\!/_{4}\,Na_2S + {}^{3}\!/_{4}\,Na_2SO_4 + {}^{1}\!/_{2}\,S_2 \tag{8}$$

15

16   XPS was used to evaluate the surface chemical states of NiAl LDO/LDS composites. Fig. 2a

17   clearly reveals that the composites are composed of Ni, Al, S, and O elements. Furthermore,

18   the element composition (at.%) of the NiAl LDO/LDS composites is depicted in Table S1.

19   The results clearly show that the existence of the S (5.06 at.%) in the NiAl LDO/LDS

20   composites. The high-resolution X-ray photoelectron spectrum of Ni 2p is shown in Fig. 2b.

21   Two spin-orbit doublets (shown at 856.1 eV and 873.9 eV) with their shakeup satellites

22   (indicated by "Sat") correspond to Ni $2p_{3/2}$ and Ni $2p_{1/2}$, and this result confirms the presence

23   of Ni^{2+}.[35] The Al 2p X-ray photoelectron spectrum (Fig. 2c) is observed at 74.2 eV,

24   suggesting the existence of Al^{3+}.[36] The O 1s peaks (Fig. S2) with the binding energies of

1   529.8 eV and 531.2 eV corresponds to the metal oxygen bonds and oxygen ions, respectively.

2   After sulfidation process, NiAl LDO/LDS composites exhibits S $2p_{3/2}$ and S $2p_{1/2}$, which are

3   shown as a strong peak at 162.3 eV and a smaller peak at 163.5 eV, respectively.[37, 38] The

4   results clearly indicate the existence of metal-sulfur bonds in the NiAl LDO/LDS composites.

5

6   Scanning electron micrographs were used to investigate the surface morphology of NiAl

7   LDH and NiAl LDO/LDS composites (Fig. 3). After the hydrothermal process, 3D

8   hierarchical architecture composed of interconnected petal-like NiAl LDH nanosheets are

9   formed (Fig. 3a and b). Ultrathin NiAl LDH nanosheets with a mean thickness of 10 nm and

10   width of ~1 μm are achieved. Such unique feature of LDH nanosheets can effectively

11   promote ion diffusion and charge transport. After sulfidation, the color of the LDH changes

12   from light green to black. Interestingly, NiAl LDO/LDS composites maintain the same

13   morphology but become more porous and dense (Figs. 3c and d). This phenomenon

14   illustrates that sulfidation not only retains the structural advantages of NiAl LDH but also

15   results in higher degree of hierarchical structure, which is beneficial to electrochemical

16   performance.

17

18   The microstructure of the NiAl LDO/LDS composites was further investigated by TEM. As

19   shown in Figs. 4a and b, the transmission electron micrographs indicate a specifically cross-

20   linked structure of NiAl LDO/LDS composites consisting of many ultrathin nanosheets. In

21   addition, TEM and AFM measurements were used as the effective means to evaluate the

22   thickness of the NiAl LDO/LDS composites. As shown in Fig. S3a, TEM image reveals that

23   the thicknesses of the petal-like NiAl LDO/LDS composites are approximately 8 to 10 nm. A

24   single piece of the NiAl LDO/LDS composites was prepared by dispersing the sample

1 powder in ethanol with sonication for 2 h prior to AFM test. The results show that the

2 thickness of the NiAl LDO/LDS sheet is approximately 7.09 nm (Fig. S3bc). The selected-

3 area electron diffraction (SAED) pattern (inset in Fig. 4b) exhibits well-defined diffraction

4 rings which are attributed to the (110) planes of Ni_3S_2 phases. This finding is consistent with

5 the XRD data. Hence, these results indicate the polycrystalline nature of the NiAl LDO/LDS

6 composites. Clear lattice fringes (Fig. 4c) show an equal interplanar distance of 0.28 nm and

7 0.23 nm corresponding to the (110) plane of Ni_3S_2 and (111) plane of NiO. To further

8 confirm the spatial distribution of chemical components, EDS mapping (Fig. 4d) shows a

9 homogeneous distribution of Ni, Al, S, and O in the NiAl LDO/LDS composites.

10

11 The electrochemical properties of the NiAl LDH and NiAl LDO/LDS electrodes were

12 evaluated using a three-electrode test. According to the NiAl LDH synthesis reaction:[39]

13 $$6Ni^{2+} + 2Al^{3+} + 16OH^- + CO_3^{2-} + 4H_2O \rightarrow Ni_6Al_2(OH)_{16}CO_3 \cdot 4H_2O \qquad (9)$$

14 Al is used to supporting the structure and does not participate in the Faradaic reactions.[40, 41]

15 The theoretical specific capacitance of NiAl LDH is contributed from $Ni(OH)_2$, which has a

16 theoretical specific capacitance of 2082 F g^{-1}.[42] Fig. 5a presents the CV curves of the NiAl

17 LDH and NiAl LDO/LDS electrodes at a scan rate of 5 mVs^{-1} in the voltage range of 0 V to

18 0.6 V (vs. SCE). Two pairs of distinct redox peaks were detected in CV curves, indicating the

19 typical pseudocapacitive nature of the electrodes. The reversible redox reactions of nickel are

20 suggested as follows: [38, 43]

21 **Faradaic redox reaction in NiAl LDH electrode**

22 $$Ni(OH)_2 + OH^- \leftrightarrow NiOOH + H_2O + e^- \qquad (10)$$
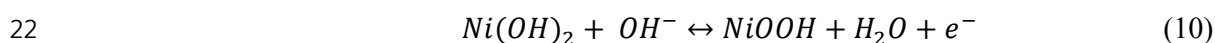
23 **Faradaic redox reaction in NiAl LDO/LDS electrode**

24 $$Ni_3S_2 + 3OH^- \leftrightarrow Ni_3S_2(OH)_3 + 3e^- \qquad (11)$$

1

2   Fig. 5a shows that the NiAl LDO/LDS electrode exhibits a larger integral area and higher

3   current density compared with the NiAl LDH electrode. These characteristics suggest the

4   improved specific capacitance caused by the improved conductivity and fast ion transport.

5   Figs. 5b and c exhibit the CV measurement of NiAl LDH and NiAl LDO/LDS electrodes at

6   various scan rates (5, 10, 20, 30, 40, 50, and 100 mV s^{-1}), respectively. The results indicate

7   that the redox peaks present small shift and without obvious shape change with increasing

8   scan rates. These characteristics signify the high reversibility of the electrode materials.[44, 45]

9   The cathodic peak current was correlated against the square root of the scan rate (Fig. 5d).

10 The NiAl LDO/LDS electrode evidently shows higher linear relationship than the NiAl LDH

11 electrode with increasing $v^{1/2}$, and this phenomenon is attributed to the rapid electrolyte

12 diffusion in the electrode.[46] The diffusion coefficients of NiAl LDO/LDS and NiAl LDH

13 electrodes were further elucidated by investigating the ion diffusion kinetics property of the

14 electrodes using the following Randles-Sevcik equation: [24, 32]

15
$$i_p = (2.69 \times 10^5)\, n^{3/2} A D_o^{1/2}\, C_o * v^{1/2} \qquad (12)$$

16 where i_p is the peak current of the electrode, n is the electron transfer number, A is the

17 electrode area, D_o is the diffusion coefficient, C_o* is the reactant concentration, and v is the

18 scan rate.

19
$$D_{LDO/LDS}/D_{LDH} = [(i_p/v^{1/2})_{LDO/LDS}/(i_p/v^{1/2})_{LDH}]^2 \qquad (13)$$

20 The results show that the diffusion coefficient of NiAl LDO/LDS electrode is 2.2 times

21 higher compared with that of the NiAl LDH electrode. Thus, the ultrathin petal-like NiAl

22 LDO/LDS composites are more favorable to ion diffusion, and this characteristic further

23 improves the electrochemical performance of the electrode.

24

1　Fig. 6a shows the GCD measurements of the NiAl LDH and NiAl LDO/LDS electrodes with

2　the potential window from 0 V to 0.4 V at a current density of 1 A g^{-1}. The different current

3　densities of the electrodes are shown in Figs. 6b and c. In this case, the nonlinear discharge

4　curves reveal the pseudocapacitance behavior attributed to the electrochemical quasi-

5　reversible redox reactions at the electrolyte–electrode interface.[5] The NiAl LDO/LDS

6　electrode displays longer discharge time, indicating higher specific capacitance. The specific

7　capacitances of NiAl LDH and NiAl LDO/LDS electrodes at different current densities are

8　demonstrated in Fig. 6d. The specific capacitance values of the NiAl LDH electrode at

9　current densities of 1, 3, 5, 8, and 10 A g^{-1} are found to be 1740.5, 1567.5, 1497.5, 1432.3,

10　and 1400.4 F g^{-1}, respectively. Similarly, the specific capacitance values of the NiAl

11　LDO/LDS electrode are 2250.5, 1567.5, 2170.5, 2047.6, 1936.7, and 1880.8 F g^{-1},

12　respectively. NiAl LDO/LDS electrode exhibits a higher specific capacitance compared with

13　NiAl LDH at the tested current density. In addition, the NiAl LDO/LDS electrode exhibits

14　higher specific capacitance compared previously reported electrode materials in literature

15　(Table S3). This phenomenon is ascribed to the increased effective active sites after

16　sulfidation.[24]

17

18　Fig. 7a shows the cycling performance of NiAl LDH and NiAl LDO/LDS electrodes at

19　different current densities. At the beginning of the first 100 cycles, the NiAl

20　LDO/LDS electrode displays a prominent specific capacitance of 2250.5 F g^{-1} at 1 A

21　g^{-1}, which is higher than that of the NiAl LDH electrode (1740.5 F g^{-1} at 1 A g^{-1}). The

22　specific capacitance gradually decreases with increasing current densities. This

23　phenomenon is ascribed to the polarization effect of the electrode during fast

24　charging/discharging.[47, 48] At low current density, abundant electrolyte ions are

1 supplied to the electrode material active sites, leading to higher specific capacitance.

2 However, at high current density, the effective interaction between the electrode

3 materials and electrolyte ions is remarkably reduced.[49] The capacitance retention of

4 NiAl LDO/LDS electrode is 97% (2180.5 F g^{-1}), which is higher than that of NiAl

5 LDH electrode (96%, 1672 F g^{-1}). The electrochemical life of the NiAl LDO/LDS

6 electrode was further investigated by performing GCD cycling measurement at the

7 current density of 5 A g^{-1} for 5000 cycles. The result indicates an excellent retention at

8 88.9% (specific capacitance of 1820.25 F g^{-1}) after 5000 cycles, which is better than

9 the NiAl LDH electrode at 83.8% (specific capacitance of 1458.54 F g^{-1}). Meanwhile,

10 the value sharply decreases at the first 300 cycles, and this reduction might be

11 attributed to the materials of the NiAl LDO/LDS electrode which tend to stabilize after

12 activation. This superior cycling performance might be due to several factors. First,

13 the special cross-linked and porous structure shortens the diffusion path which

14 ascertains the rapidly ion diffusion kinetics. Second, sulfidation transforms the metal

15 oxide to metal sulfide species Ni_3S_2, which supplies additional electrochemical active

16 sites for Faradic redox reaction.[50] Finally, the sulfidation increases the internal

17 conductivity of electrode materials which enhances the electrochemical stability.[51]

18 Moreover, the NiAl LDO/LDS electrode remains the Coulombic efficiency of 94.1%

19 at a current density of 5 A g^{-1} during 5000 charge-discharge cycles, which is higher

20 than that of the NiAl LDH electrode (88.2%) (Fig. S4).

21

22 EIS analysis was further performed to measure the internal resistances and charge transfer

23 kinetics of the electrode for SCs.[52] Fig. 7c shows the EIS curves and fitted results of the NiAl

24 LDH and NiAl LDO/LDS electrodes based on the equivalent circuit depicted in the inset of

1   Fig. 7c. The equivalent circuit was used to measure the impedance properties of the

2   electrodes. These properties include the internal resistance (R_s), Faradic charge transfer

3   resistance (R_{ct}), Warburg diffusion element (Z_w), double layer capacitance (C_{dl}), and

4   pseudocapacitance (C_F).[36, 53, 54] Originally, the Nyquist plots displays a semicircle in the high-

5   frequency region which can be attributed to charge transfer process between the electrode

6   materials and electrolyte. Subsequently, a sloped line is observed in the low-frequency region,

7   and this result suggests the electrolyte ion diffusion in the electrode materials.[55] According to

8   the result, the intercept on the real impedance z' axis at the high-frequency region represents

9   the internal resistance (R_s), which includes the intrinsic resistance of the electrode materials,

10 resistance of KOH electrolyte, and the contact resistance at the active electrode material and

11 nickel foam interface.[5] The NiAl LDO/LDS electrode shows a smaller semicircle and a

12 steeper slope compared with the NiAl LDH electrode. The impedance result of the two

13 electrodes was obtained from the complex nonlinear least square fitting as shown in Table S2.

14 The results show that the NiAl LDO/LDS electrode exhibits lower internal resistance (0.499

15 Ω) and charge transfer resistance (0.308 Ω) than the NiAl LDH electrode (0.665 Ω and 12.53

16 Ω).

17

18 Fig. 8a presents the CV curves of graphene and NiAl LDO/LDS composites electrodes at the

19 scan rate of 5 mV s^{-1}. The graphene electrode displays a typical rectangular curve at the

20 voltage range from -1 V to 0 V, whereas NiAl LDO/LDS composites electrode exhibits a

21 pseudocapacitive characteristic at the voltage range from 0 V to 0.6 V. These characteristics

22 result in a wide potential window of 1.6 V. CV curves of NiAl LDO/LDS//G ASC display

23 similar non-rectangular capacitive behavior at various scan rates of 5, 10, 20, 30, 50 and 100

24 mV s^{-1} between 0 V and 1.6 V (Fig. 8b), suggesting good electrochemical reversibility and

1   high rate capability of the ASC. The CV curves in Fig. 8b show a non-rectangular capacitive

2   behavior. This is because the potential window of the NiAl LDO/LDS//G ASC is composed

3   of electric double layer capacitance and Faradaic redox behaviors, which agrees well with

4   similar reports.[8, 56] The GCD curves of NiAl LDO/LDS//G ASC (Fig. 8c.) depict small

5   voltage loss (IR drop) in the device, revealing a low internal resistance of the ASC device.

6   Fig. 8d shows the specific capacitance of the NiAl LDO/LDS//G ASC delivering high

7   specific capacitances of 153.3, 82.8, 70.67, 61.87, and 60 F g^{-1} at 1, 3, 5, 8, and 10 A g^{-1},

8   respectively. The NiAl LDO/LDS//G ASC retains 95.68% of its initial specific capacitance at

9   5 A g^{-1} after 5000 charge-discharge cycles (Fig. 8e), indicating good electrochemical stability.

10   In addition, the Coulombic efficiency of the device remains at 86.7%, indicating an excellent

11   reversibility.[57, 58] Fig. 8f displays the Ragone plot of NiAl LDO/LDS//G ASC with high

12   energy density of 47.9 Wh kg^{-1} at a power density of 750 W kg^{-1}. This impressive energy

13   density is obviously larger than those of other reported ASC devices, such as NiAl

14   LDH/GNS//GNS (31.5 Wh kg^{-1} at 400 W kg^{-1}),[59] NiO//CNTs (27.8 Wh kg^{-1} at 700 W

15   kg^{-1}),[60] NiO//C (19 Wh kg^{-1} at 32 W kg^{-1}),[61] $Ni(OH)_2$ (36.2 Wh kg^{-1} at 100.6 W kg^{-1}),[62]

16   $Ni(OH)_2$@3D Ni//AC (21.8 Wh kg^{-1} at 660 W kg^{-1}),[63] and NiCo LDH//AC (23.7 Wh kg^{-1} at

17   248 W kg^{-1}).[64]

18

19   **Conclusions**

20   In conclusion, petal-like porous NiAl LDO/LDS composites material has been fabricated

21   through a facile hydrothermal method followed by sulfidation process. The as-fabricated

22   NiAl LDO/LDS electrode exhibits excellent supercapacitor performance with specific

23   capacitance of 2250.5 F g^{-1} at 1 A g^{-1} and remarkable cycling stability compared with NiAl

24   LDH electrode (1740.5 F g^{-1} at 1 A g^{-1}). The ultrathin nanoplate morphology and sulfide

1　content account for the impressive electrochemical performance. Finally, the NiAl

2　LDO/LDS//G ASC device delivers high energy density of 47.9 Wh kg^{-1} at a power density of

3　750 W kg^{-1} with exceptional cycling stability of 95.68% cell capacitance retention after 5000

4　cycles. This work highlights a simple sulfidation approach to synthesize sulfidized LDH

5　material with high cycling stability for high-performance supercapacitors.

6

7　**Acknowledgements**

12

13

14

15

16

17

18

19

20

21

22

23

24

1

2

3

4

5

6

7

8

9 **References**

10   1.   C. Yuan, H. B. Wu, Y. Xie and X. W. D. Lou, *Angew. Chem. Int. Ed.*, 2014, **53**, 1488.

11   2.   J. Yang, C. Yu, X. Fan and J. Qiu, *Adv. Energy Mater.*, 2014, **4**, 1400761.

12   3.   M. Winter and R. J. Brodd, *Chem. Rev.*, 2004, **104**, 4245-4269.

13   4.   J. R. Miller and P. Simon, *Science*, 2008, **321**, 651-652.

14   5.   L. J. Zhang, J. Wang, J. J. Zhu, X. G. Zhang, K. S. Hui and K. N. Hui, *J. Mater. Chem.*

15   *A*, 2013, **1**, 9046-9053.

16   6.   Z. Li, M. Shao, L. Zhou, R. Zhang, C. Zhang, J. Han, M. Wei, D. G. Evans and X.

17   Duan, *Nano Energy*, 2016, **20**, 294-304.

18   7.   L. Zhang, K. N. Hui, K. S. Hui and H. Lee, *Electrochim. Acta*, 2015, **186**, 522-529.

19   8.   H. Lai, Q. Wu, J. Zhao, L. Shang, H. Li, R. Che, Z. Lyu, J. Xiong, L. Yang and X.

20   Wang, *Energy Environ. Sci.*, 2016, **9**, 2053-2060.

21   9.   M. F. Shao, R. K. Zhang, Z. H. Li, M. Wei, D. G. Evans and X. Duan, *Chem.*

22   *Commun.*, 2015, **51**, 15880-15893.

23   10.   J. Xu, F. He, S. L. Gai, S. H. Zhang, L. Li and P. P. Yang, *Nanoscale*, 2014, **6**, 10887-

24   10895.

1   11.   L. Zhang, K. N. Hui, K. S. Hui and H. Lee, *Electrochim. Acta*, 2015, **186**, 522-529.

2   12.   F. Ning, M. Shao, C. Zhang, S. Xu, M. Wei and X. Duan, *Nano Energy*, 2014, **7**, 134-

3   142.

4   13.   L. Yan, R. Li, Z. Li, J. Liu, Y. Fang, G. Wang and Z. Gu, *Electrochim. Acta*, 2013, **95**,

5   146-154.

6   14.   L. J. Zhang, X. G. Zhang, L. F. Shen, B. Gao, L. Hao, X. J. Lu, F. Zhang, B. Ding and

7   C. Z. Yuan, *J. Power Sources*, 2012, **199**, 395-401.

8   15.   J. P. Cheng, J. H. Fang, M. Li, W. F. Zhang, F. Liu and X. B. Zhang, *Electrochim.*

9   *Acta*, 2013, **114**, 68-75.

10   16.   G. H. Cheng, W. F. Yang, C. Q. Dong, T. Y. Kou, Q. G. Bai, H. Wang and Z. H. Zhang,

11   *J. Mater. Chem. A*, 2015, **3**, 17469-17478.

12   17.   S. X. Wu, K. S. Hui, K. N. Hui and K. H. Kim, *J. Mater. Chem. A*, 2016, **4**, 9113-9123.

13   18.   Q. Yang, Z. Y. Lu, X. M. Sun and J. F. Liu, *Sci. Rep.*, 2013, **3**, 3537.

14   19.   C. Z. Yuan, J. Y. Li, L. R. Hou, X. G. Zhang, L. F. Shen and X. W. Lou, *Adv. Funct.*

15   *Mater.*, 2012, **22**, 4592-4597.

16   20.   Y. Q. Zhu, C. B. Cao, S. Tao, W. S. Chu, Z. Y. Wu and Y. D. Li, *Sci. Rep.*, 2014, **4**,

17   5787.

18   21.   X. Y. Yu, L. Yu, L. F. Shen, X. H. Song, H. Y. Chen and X. W. Lou, *Adv. Funct. Mater.*,

19   2014, **24**, 7440-7446.

20   22.   Y. M. Chen, Z. Li and X. W. Lou, *Angew. Chem. Int. Ed.*, 2015, **54**, 10521-10524.

21   23.   J. Pu, T. T. Wang, H. Y. Wang, Y. Tong, C. C. Lu, W. Kong and Z. H. Wang,

22   *Chempluschem*, 2014, **79**, 577-583.

23   24.   H. Hua, S. J. Liu, Z. Y. Chen, R. Q. Bao, Y. Y. Shi, L. R. Hou, G. Pang, K. N. Hui, X.

24   G. Zhang and C. Z. Yuan, *Sci. Rep.*, 2016, **6**, 20973.

Journal of Materials Chemistry A Accepted Manuscript

1   25.   L. Lu, H.-y. Wang, J.-G. Wang, C. Wang and Q.-C. Jiang, *J. Mater. Chem. A*, 2017, **5**,

2   2530-2538.

3   26.   J. Hong, Y.-W. Lee, D. Ahn, S. Pak, J. Lee, A.-R. Jang, S. Lee, B. Hou, Y. Cho and S.

4   M. Morris, *Nano Energy*, 2017, **39**, 337-345.

5   27.   R. O. WILLIAMS . HUMMERS JR., *J. Am. Chem. Soc.*, 1958, **80**, 1339.

6   28.   N. I. Kovtyukhova, P. J. Ollivier, B. R. Martin, T. E. Mallouk, S. A. Chizhik, E. V.

7   Buzaneva and A. D. Gorchinskiy, *Chem. Mater.*, 1999, **11**, 771-778.

8   29.   H. Liang, C. Xia, Q. Jiang, A. N. Gandi, U. Schwingenschlögl and H. N. Alshareef,

9   *Nano Energy*, 2017, **35**, 331-340.

10   30.   L. J. Zhang, K. N. Hui, K. S. Hui, X. Chen, R. Chen and H. W. Lee, *Int. J. Hydrogen*

11   *Energy*, 2016, **41**, 9443-9453.

12   31.   L. Li, K. San Hui, K. N. Hui, Q. Xia, J. Fu and Y.-R. Cho, *J. Alloys Compd.* , 2017,

13   **721**, 803-812.

14   32.   Q. X. Xia, K. S. Hui, K. N. Hui, S. D. Kim, J. H. Lim, S. Y. Choi, L. J. Zhang, R. S.

15   Mane, J. M. Yun and K. H. Kim, *J. Mater. Chem. A*, 2015, **3**, 22102-22117.

16   33.   L. W. Mi, Q. Ding, W. H. Chen, Z. Zheng, H. W. Hou, C. T. Liu and C. Y. Shen, *RSC*

17   *Adv.*, 2012, **2**, 6817-6823.

18   34.   S. J. Peng, L. L. Li, H. T. Tan, R. Cai, W. H. Shi, C. C. Li, S. G. Mhaisalkar, M.

19   Srinivasan, S. Ramakrishna and Q. Y. Yan, *Adv. Funct. Mater.*, 2014, **24**, 2155-2162.

20   35.   H. Pang, C. Z. Wei, X. X. Li, G. C. Li, Y. H. Ma, S. J. Li, J. Chen and J. S. Zhang, *Sci.*

21   *Rep.*, 2014, **4**, 3577.

22   36.   J. Memon, J. H. Sun, D. L. Meng, W. Z. Ouyang, M. A. Memon, Y. Huang, S. K. Yan

23   and J. X. Geng, *J. Mater. Chem. A*, 2014, **2**, 5060-5067.

24   37.   Y. J. Ruan, J. J. Jiang, H. Z. Wan, X. Ji, L. Miao, L. Peng, B. Zhang, L. Lv and J. Liu,

1   *J. Power Sources*, 2016, **301**, 122-130.

2   38.   Z. Zhang, Q. Wang, C. Zhao, S. Min and X. Qian, *ACS Appl. Mater. Inter.*, 2015, **7**,

3   4861-4868.

4   39.   S. X. Wu, K. S. Hui and K. N. Hui, *J. Phys. Chem. C*, 2015, **119**, 23358-23365.

5   40.   D. Du, X. Wu, S. Li, Y. Zhang, W. Xing, L. Li, Q. Xue, P. Bai and Z. Yan, *J. Mater.*

6   *Chem. A*, 2017, **5**, 8964-8971.

7   41.   L. Zhang, R. Chen, K. N. Hui, K. San Hui and H. Lee, *Chem. Eng. J.*, 2017, **325**, 554-

8   563.

9   42.   J. Yan, Z. J. Fan, W. Sun, G. Q. Ning, T. Wei, Q. Zhang, R. F. Zhang, L. J. Zhi and F.

10   Wei, *Adv. Funct. Mater.*, 2012, **22**, 2632-2641.

11   .43.   J. C. Xing, Y. L. Zhu, Q. W. Zhou, X. D. Zheng and Q. J. Jiao, *Electrochim. Acta*,

12   2014, **136**, 550-556.

13   44.   K. Karthikeyan, S. Amaresh, V. Aravindan, H. Kim, K. S. Kang and Y. S. Lee, *J.*

14   *Mater. Chem. A*, 2013, **1**, 707-714.

15   45.   Y. Zhao, X. Zhang, J. He, L. Zhang, M. Xia and F. Gao, *Electrochim. Acta*, 2015, **174**,

16   51-56.

17   46.   B. Liu, H. T. Yuan, Y. S. Zhang, Z. X. Zhou and D. Y. Song, *J. Power Sources*, 1999,

18   **79**, 277-280.

19   47.   H. Ma, J. He, D.-B. Xiong, J. Wu, Q. Li, V. Dravid and Y. Zhao, *ACS Appl. Mater.*

20   *Inter.,* 2016, **8**, 1992-2000.

21   48.   Y. Zhao, H. Ma, S. Huang, X. Zhang, M. Xia, Y. Tang and Z.-F. Ma, *ACS Appl. Mater.*

22   *Inter.*, 2016, **8**, 22997-23005.

23   49.   K. B. Xu, R. J. Zou, W. Y. Li, Q. Liu, X. J. Liu, L. An and J. Q. Hu, *J. Mater. Chem. A*,

24   2014, **2**, 10090-10097.

Journal of Materials Chemistry A Accepted Manuscript

1   50.   Y. Lu, B. Jiang, L. Fang, F. Ling, F. Wu, B. Hu, F. Meng, K. Niu, F. Lin and H. Zheng,

2   *J. Alloys Compd.* , 2017, **714**, 63-70.

3   51.   B. Yang, L. Yu, Q. Liu, J. Liu, W. Yang, H. Zhang, F. Wang, S. Hu, Y. Yuan and J.

4   Wang, *CrystEngComm*, 2015, **17**, 4495-4501.

5   52.   Y. F. Xu, M. G. Schwab, A. J. Strudwick, I. Hennig, X. L. Feng, Z. S. Wu and K.

6   Mullen, *Adv. Energy Mater.*, 2013, **3**, 1035-1040.

7   53.   X. Wang, C. Y. Yan, A. Sumboja and P. S. Lee, *Nano Energy*, 2014, **3**, 119-126.

8   54.   B. Wang, Q. Liu, Z. Y. Qian, X. F. Zhang, J. Wang, Z. S. Li, H. J. Yan, Z. Gao, F. B.

9   Zhao and L. H. Liu, *J. Power Sources*, 2014, **246**, 747-753.

10   55.   F. L. Lai, Y. E. Miao, Y. P. Huang, T. S. Chung and T. X. Liu, *J. Phys. Chem. C*, 2015,

11   **119**, 13442-13450.

12   56.   X. Ren, C. Guo, L. Xu, T. Li, L. Hou and Y. Wei, *ACS Appl. Mater. Inter.*, 2015, **7**,

13   19930-19940.

14   57.   J. Lin, Y. Liu, Y. Wang, H. Jia, S. Chen, J. Qi, C. Qu, J. Cao, W. Fei and J. Feng, *J.*

15   *Power Sources*, 2017, **362**, 64-72.

16   58.   B. Wei, H. Liang, D. Zhang, Z. Wu, Z. Qi and Z. Wang, *J Mater Chem A*, 2017, **5**,

17   2844-2851.

18   59.   L. J. Zhang, K. N. Hui, K. S. Hui, X. Chen, R. Chen and H. Lee, *Int. J. Hydrogen*

19   *Energy*, 2016, **41**, 13329-13329.

20   60.   H. W. Wang, H. Yi, X. Chen and X. F. Wang, *Electrochim. Acta*, 2013, **105**, 353-361.

21   61.   D. W. Wang, F. Li and H. M. Cheng, *J. Power Sources*, 2008, **185**, 1563-1568.

22   62.   J. C. Huang, P. P. Xu, D. X. Cao, X. B. Zhou, S. N. Yang, Y. J. Li and G. L. Wang, *J.*

23   *Power Sources*, 2014, **246**, 371-376.

24   63.   Y. Z. Su, K. Xiao, N. Li, Z. Q. Liu and S. Z. Qiao, *J. Mater. Chem. A*, 2014, **2**, 13845-

1　　　　13853.

2　　64.　　X. Wang, A. Sumboja, M. F. Lin, J. Yan and P. S. Lee, *Nanoscale*, 2012, **4**, 7266-7272.

3

4

5

6

7

8

9

10　　**Scheme 1** Illustration of the formation of petal-like NiAl LDH and NiAl LDO/LDS

11　　composites.

12　　**Fig. 1** X-ray diffraction patterns of (a) NiAl LDH and (b) NiAl LDO/LDS composites.

13　　**Fig. 2** X-ray photoelectron spectra of NiAl LDO/LDS composites: (a) full spectrum, (b) Ni

14　　2p, (c) Al 2p, and (d) S 2p.

15　　**Fig. 3** Field-emission scanning electron micrographs of the (a, b) NiAl LDH and (c, d) NiAl

16　　LDO/LDS composites.

17　　**Fig. 4** (a, b) Transmission electron micrographs (inset in b) the corresponding SAED pattern,

18　　and (c) high-resolution transmission electron micrograph and (d) Energy dispersive X-ray

19　　spectral mapping of the NiAl LDO/LDS composites.

20　　**Fig. 5** Cyclic voltammograms of (a) NiAl LDO/LDS and NiAl LDH electrodes at the scan

21　　rate of 5 mV s^{-1} and (b) NiAl LDH electrode and (c) NiAl LDO/LDS electrode at different

22　　scan rates. (d) Linear relationship between the cathodic peak current and square root of the

23　　scan rate.

24　　**Fig. 6** Galvanic change-discharge curves of (a) NiAl LDO/LDS and NiAl LDH at a current

1   density of 1 A g^{-1}, and (b) NiAl LDH electrode and (c) NiAl LDO/LDS electrode at different

2   current densities. (d) Specific capacitances of NiAl LDH and NiAl LDO/LDS electrodes at

3   different current densities.

4   **Fig. 7** Cycling performances of (a) NiAl LDO/LDS and NiAl LDH electrodes at different

5   current densities and (b) the petal-like NiAl LDO/LDS composites at a current density of 5 A

6   g^{-1}. (c) Nyquist plots of the NiAl LDO/LDS and NiAl LDH electrodes.

7   **Fig. 8** Cyclic voltammograms of (a) graphene and NiAl LDO/LDS at a scan rate of 5 mV s^{-1}

8   and (b) NiAl LDO/LDS//G ASC device at different scan rate. (c) GCD curves of NiAl

9   LDO/LDS//G ASC device at different current densities, (d) Specific capacitances of NiAl

10   LDO/LDS//G ASC device at different current densities. (e) Cycling performance and

11   Coulombic efficiency of LDO/LDS//G ASC device at 5 A g^{-1}. (f) Ragone plot of NiAl

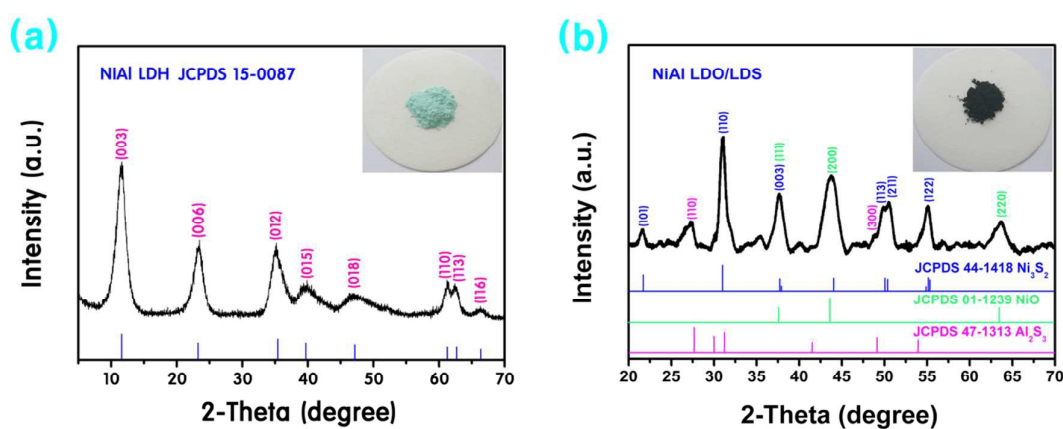12   LDO/LDS//G ASC device.

13

14

15

16

17

18

19

20

21

22

23

24

1

2

3

4

5

6

7

8
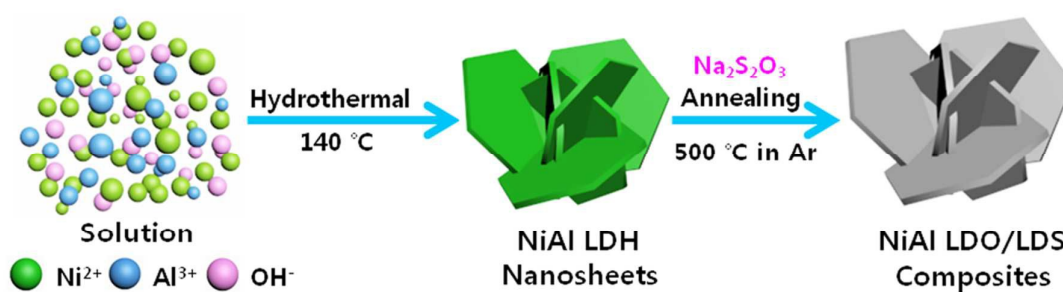
9   **Scheme 1** Illustration of the formation of petal-like NiAl LDH and NiAl LDO/LDS

10   composites.

11

12

13

14

15

16

17

18

19

20

1

2

3

4

5

6

7

8

9

Fig. 1 X-ray diffraction patterns of (a) NiAl LDH and (b) NiAl LDO/LDS composites.
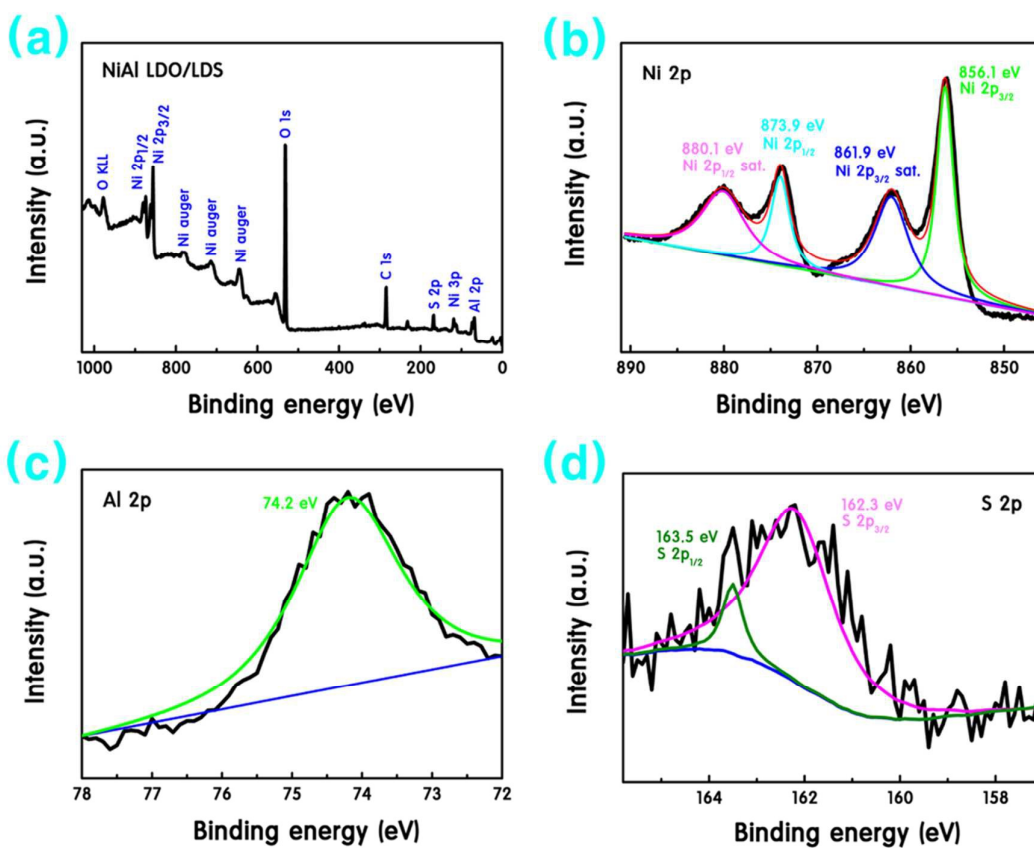
11

12

13

14

15

16

17

18

Journal of Materials Chemistry A Accepted Manuscript

1

2

3

4

5

6

7

Fig. 2 X-ray photoelectron spectra of NiAl LDO/LDS composites: (a) full spectrum, (b) Ni

2p, (c) Al 2p, and (d) S 2p.

10
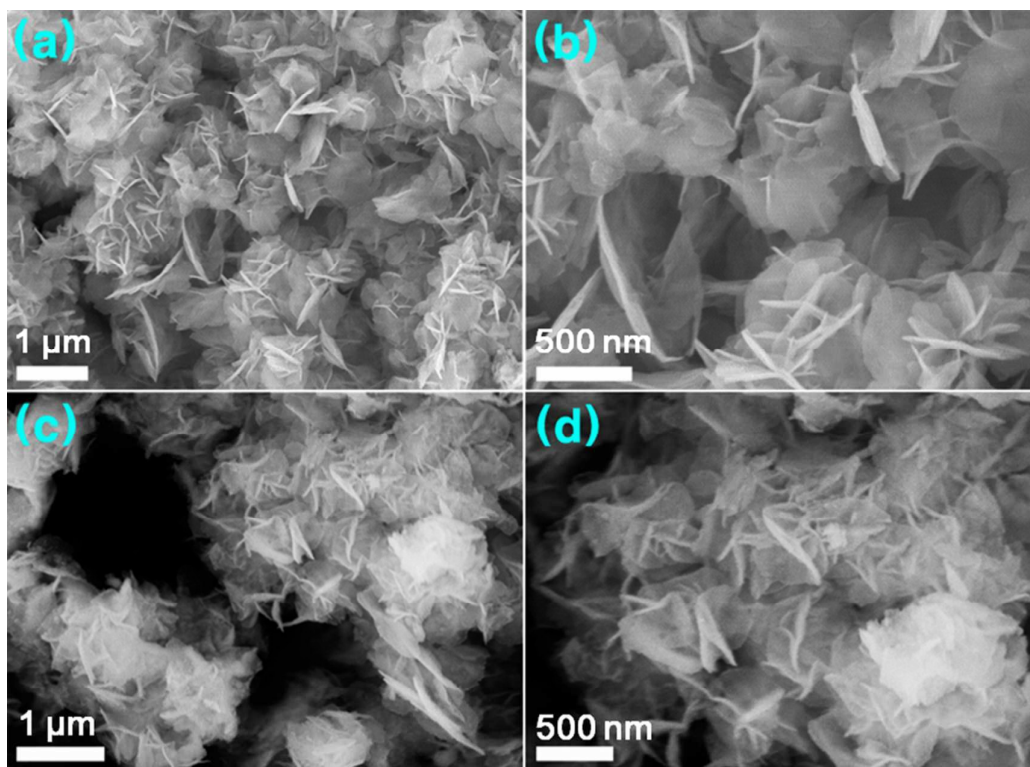
11

12

Fig. 3 Field-emission scanning electron micrographs of the (a, b) NiAl LDH and (c, d) NiAl LDO/LDS composites.

1

2

3

4

5

6

7
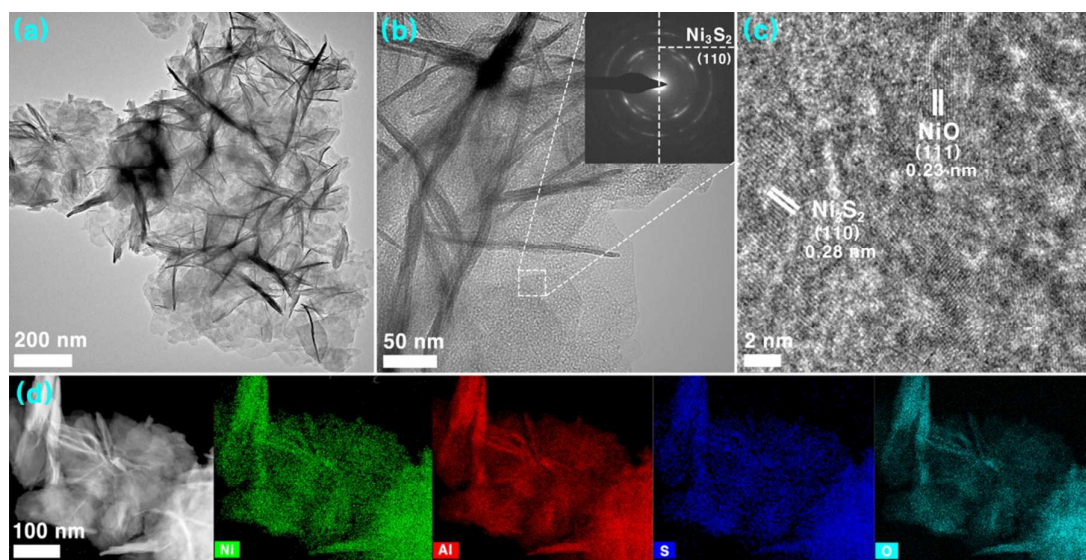
Fig. 4 (a, b) Transmission electron micrographs (inset in b) the corresponding SAED pattern,

and (c) high-resolution transmission electron micrograph and (d) Energy dispersive X-ray

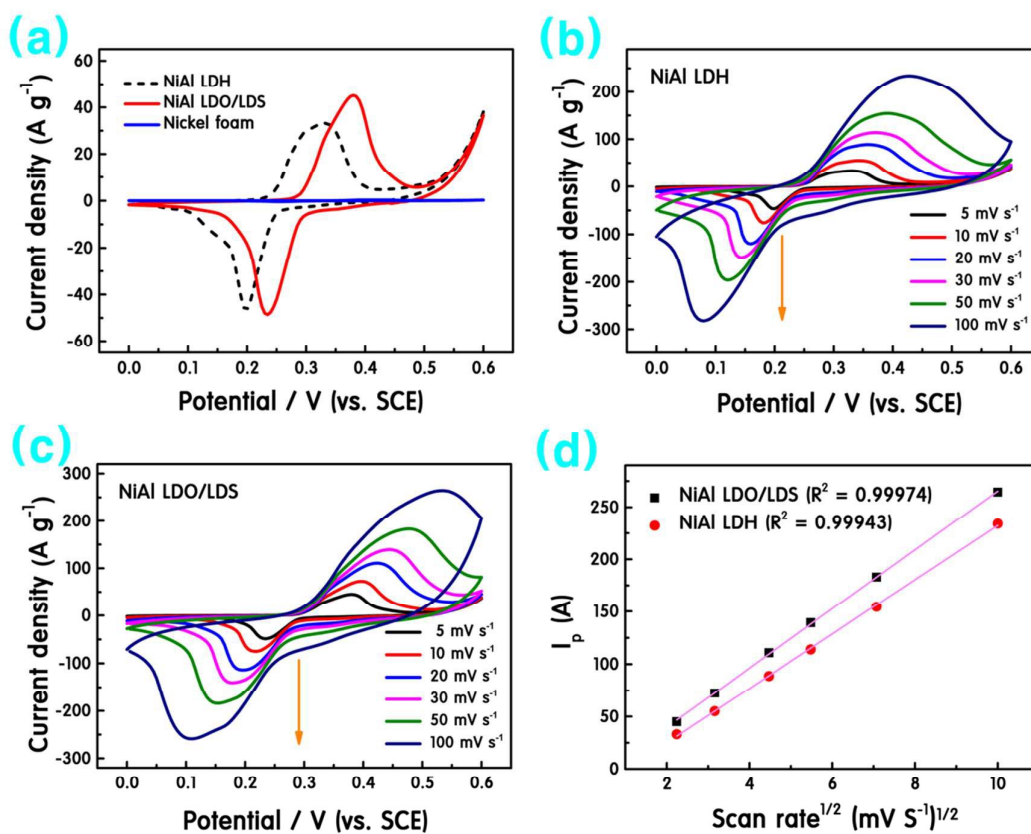spectral mapping of the NiAl LDO/LDS composites.

11

12

13

14

15

16

17

1

2

3

4

5

6

7

Fig. 5 Cyclic voltammograms of (a) NiAl LDO/LDS and NiAl LDH electrodes at the scan

rate of 5 mV·s^{-1} and (b) NiAl LDH electrode and (c) NiAl LDO/LDS electrode at different

scan rates. (d) Linear relationship between the cathodic peak current and square root of the
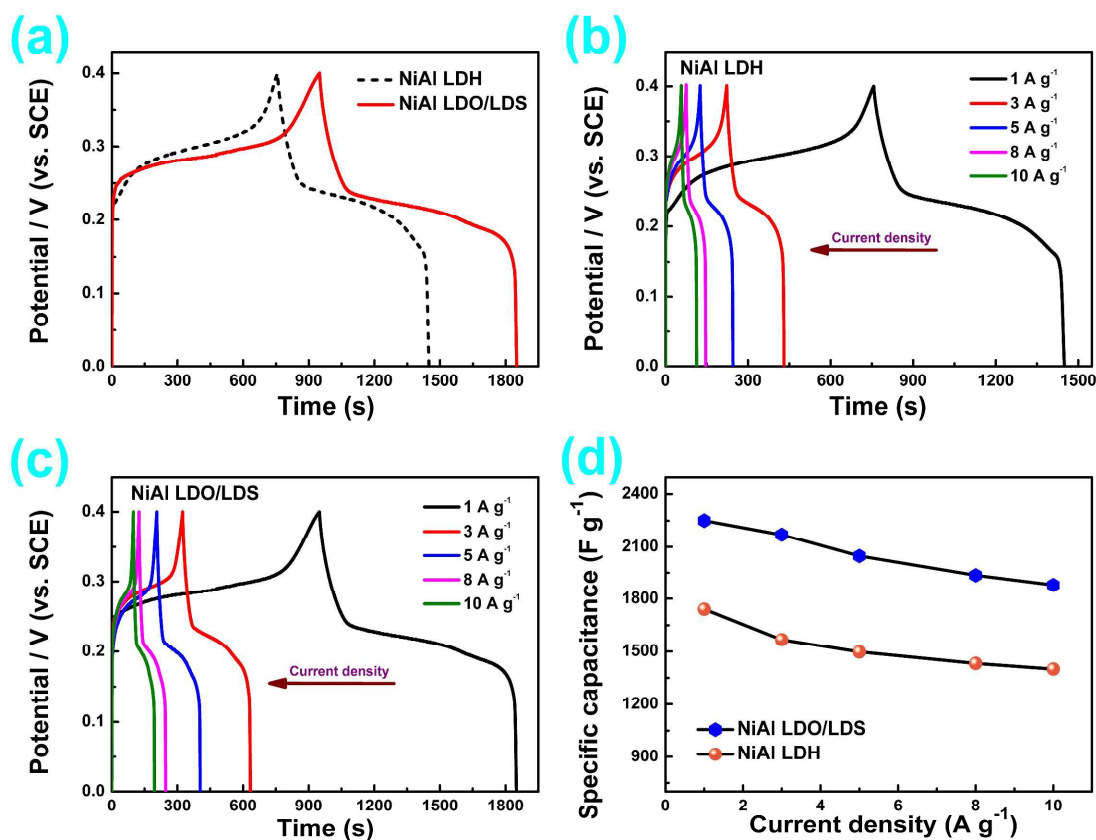
scan rate

12

1

2

3

4

5

6

7

Fig. 6 Galvanic change-discharge curves of (a) NiAl LDO/LDS and NiAl LDH at a current

density of 1 A g^{-1}, and (b) NiAl LDH electrode and (c) NiAl LDO/LDS electrode at different

current densities. (d) Specific capacitances of NiAl LDH and NiAl LDO/LDS electrodes at
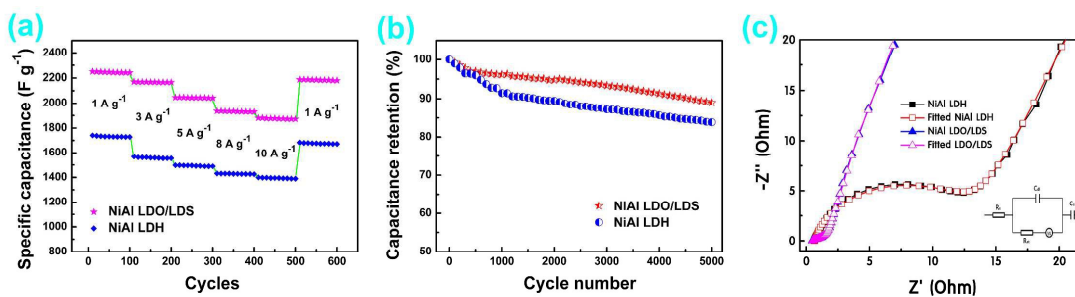
different current densities.

12

13

Fig. 7 Cycling performances of (a) NiAl LDO/LDS and NiAl LDH electrodes at different current densities and (b) the petal-like NiAl LDH and NiAl LDO/LDS composites at a current density of 5 A g^{-1}. (c) Nyquist plots of the NiAl LDO/LDS and NiAl LDH electrodes.
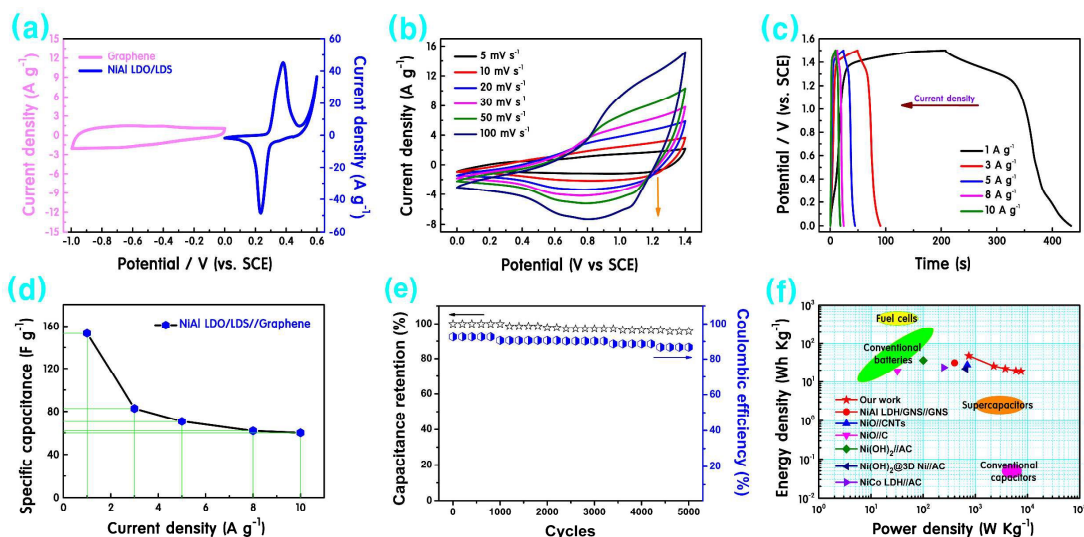
32

1

2

3

4

5

6

Fig. 8 Cyclic voltammograms of (a) graphene and NiAl LDO/LDS at a scan rate of 5 mV s^{-1}

and (b) NiAl LDO/LDS//G ASC device at different scan rate. (c) GCD curves of NiAl

LDO/LDS//G ASC device at different current densities, (d) Specific capacitances of NiAl

LDO/LDS//G ASC device at different current densities. (e) Cycling performance and

Coulombic efficiency of NiAl LDO/LDS//G ASC device at 5 A g^{-1}. (f) Ragone plot of NiAl

LDO/LDS//G ASC device

13

14

15